

Three-dimensional multi-mesh material point method for solving collision problems

PAN Xiaofei, XU Aiguo, ZHANG Guangcai and ZHU Jianshi

Laboratory of Computational Physics,

Institute of Applied Physics and Computational Mathematics,

P. O. Box 8009-26, Beijing 100088, P. R. China

MA Shang and ZHANG Xiong

School of Aerospace, Tsinghua University, Beijing 100084, P. R. China

(Dated: October 30, 2018)

Abstract

Contact algorithm between different bodies plays an important role in solving collision problems. Usually it is not easy to be treated very well. Several ones for material point method were proposed by Bardenhagen, Brackbill, and Sulsky[13, 14], Hu and Chen[18]. An improved one for three-dimensional material point method is presented in this paper. The improved algorithm emphasizes the energy conservation of the system and faithfully recovers opposite acting forces between contacting bodies. Contrasted to the one by Bardenhagen, both the normal and tangential contacting forces are more appropriately applied to the contacting bodies via the contacting nodes of the background mesh; Contrasted to the one by Hu and Chen, not only the tangential velocities but also the normal ones are handled separately in respective individual mesh. This treatment ensures not only the contact/sliding/separation procedure but also the friction between contacting bodies are recovered. The presented contact algorithm is validated via numerical experiments including rolling simulation, impact of elastic spheres, impact of a Taylor bar and impact of plastic spheres. The numerical results show that the multi-mesh material point method with the improved contact algorithm is more suitable for solving collision problems.

PACS numbers: 02.70.Dh; 02.60.Cb; 02.70.Ns; 02.60.Jh

Keywords: material-point method(MPM); energy conservation; contact algorithm; multi-mesh

Supported by National Natural Science Foundation of China (contract number: 10472052) and Science Foundation of National Key Laboratory of Computational Physics, Institute of Applied Physics and Computational Mathematics, Beijing, China.

I. INTRODUCTION

Phenomena with large deformation and/or large rotation are very common in nature, especially in fields of hypervelocity impact and explosion. Numerical simulations of such processes are necessary and challenging. The material point method(MPM) is an extension of FLIP[1, 2] which combines the strength of Eulerian and Lagrangian descriptions of the material, to the solid mechanics. The Lagrangian description is provided by discretizing each body by a collection of material points, and the Eulerian description is based on a background computational mesh. Information carried by the material points is projected on to the background mesh where equations of motion are solved. The mesh solution is then used to update the material points. In Sulsky et al[3, 6] a weak formulation of the MPM algorithm for solid mechanics is given and the method is framed in the terms of finite elements. The MPM combines the advantages of Eulerian and Lagrangian methods, which can avoid the distortion of Lagrangian mesh and track the boundaries of bodies. The method has been applied to the large strain problems[7, 8], calculations with dynamical energy release rate[11], fracture mechanics[12], dynamics failure[4, 5], hypervelocity impact[9], the thin membranes[10], granular materials[13, 15, 16, 17] etc.

In MPM, no slip contact between bodies is contained in the basic algorithm without additional cost. But at most cases separation or sliding may happen during the moving of bodies. A contact algorithm was presented by Bardenhagen, Brackbill and Sulsky to simulate the interactions of the grains of granular material[13]. In the algorithm, the contact may occur if the material points of different bodies are projected on to the same nodes of the background mesh, and the contact force is associated with the center-of-mass velocity. Bardenhagen's algorithm is linear in the number of grains and allows separation, sliding and rolling. With the contact algorithm MPM has been successful in simulating the large deformation of shear in granular material, having an advantage over traditional finite element methods(FEM) in that the use of regular grid eliminates the necessity to do costly search for contact surfaces. In order to apply MPM to stress propagation in the granular material, the contact algorithm is improved by Bardenhagen et al[14]. In Bardenhagen's improved contact algorithm, the normal traction is included in the contact logic to more appropriately determine the free separation criterion.

To release the no-slip contact algorithm in MPM, a multi-mesh mapping scheme is proposed by Hu and Chen[18]. In the multi-mesh mapping scheme, each material lies in an individual background mesh rather than in the common background mesh. The meshing process of spur gears is simulated by Hu and Chen with their contact algorithm. To avoid interpenetration and allow separation in the gear meshing process, the normal velocity of any particle at the contact surface is calculated in the common background mesh, while the tangential velocity is found based on the corresponding information in respective individual mesh. With the proposed contact algorithm, Hu and Chen have successfully simulated the contact and separation of the gears. In their scheme, normal acceleration is set to be equal if particles of different bodies are mapped on the same node. But for some cases, the bodies may

separate although their particles are still mapped on the same nodes, which can cause energy dissipation during contact. In the contact algorithm by Hu and Chen, the friction between different bodies is completely ignored because the tangential velocities of different bodies are assumed to be independent.

In this paper, an improved multi-mesh contact algorithm for three-dimensional MPM is proposed. In the present contact algorithm, the criterion of contact condition is similar to Bardengen’s which ensures that the search for the contact of different bodies is fast, but the multi-mesh is used to calculate the normal and tangential velocities of different bodies. To avoid interpenetration the normal contact force is calculated at the contact surface and the Coulomb friction is applied in the tangential direction. Contrasting with Bardenhagen’s algorithm, both the normal and tangential contacting force are more appropriately applied to the contacting bodies at the contacting nodes of the background mesh; Contrasting with Hu and Chen’s contact algorithm, the normal velocities of different bodies are deal with separately just as the tangential velocities to not only ensure the contact/sliding/separation procedure can be simulated but also ensure the friction between different bodies can be applied. With the presented algorithm the total energy of the system is nearly constant during both elastic and non-elastic collision procedures, which shows numerical energy dissipation is little.

This paper is organized as follows. The material point method is briefly reviewed in section II, and the new multi-mesh contact algorithm is illuminated in Section III. Several numerical examples are presented In section IV to validate the interaction between bodies with the contact algorithm. Numerical results obtained by the proposed contact algorithm presented are compared with those obtained by Bardenhagen’s contact algorithm which show the proposed algorithm is more suitable in solving collision problems in which the numerical energy dissipation need to be very low. Section V concludes the paper with some remarks and observations.

II. THE MATERIAL POINT METHOD

The MPM is a particle method based on particle-in-cell(PIC) method in computational fluid mechanics. The method was initially developed for and has been successfully applied in problems involving large-deformation, large rotations of solid, etc. For continuum bodies, the conservation equation for mass is

$$\frac{d\rho}{dt} + \rho \nabla \cdot \mathbf{v} = 0. \quad (1)$$

And for pure mechanical problems the differential equation of balance is

$$\rho \frac{d\mathbf{v}}{dt} = \nabla \cdot \sigma + \rho \mathbf{b}, \quad (2)$$

where ρ is the mass density, \mathbf{v} is the velocity, σ is the stress tensor and \mathbf{b} is the body force.

The formulation (2) is solved in a Lagrangian frame on a finite element mesh. The Lagrangian formulation means that the momentum equation does not contain the convection term which can cause significant numerical error in pure Eulerian approaches.

In MPM, the continuum bodies are discretized with N_p material particles. Each material particle carries the information of position, velocity, mass, density, stress, strain and all other internal state variables necessary for the constitutive model. Since the mass of each material particle is equal and fixed, Eq. (1) is automatically satisfied. At each time step, the mass and velocities of the material particles are mapped onto the background computational mesh(grid). The mapped nodal velocity \mathbf{v}_j is obtained through the following equation,

$$\sum_j m_{ij} \mathbf{v}_j = \sum_p m_p \mathbf{v}_p N_i(\mathbf{x}_p) \quad (3)$$

where m_p , \mathbf{v}_p and \mathbf{x}_p are the mass, velocity and position of particle p , separately. N_i is the element shape function, i and j indexes of node. For three-dimensional problem, a eight-node cell is employed with the shape functions given by

$$N_i = \frac{1}{8}(1 + \xi\xi_i)(1 + \eta\eta_i)(1 + \zeta\zeta_i) \quad (4)$$

where ξ , η and ζ are the natural coordinates of a material particle in the cell along the x-, y- and z-directions, ξ_i , η_i and ζ_i are the natural coordinates of the node i in the cell along the three directions.

In the Eq. (3), the consistent mass matrix, m_{ij} , is

$$m_{ij} = \sum_p m_p N_i(\mathbf{x}_p) N_j(\mathbf{x}_p) \quad (5)$$

In practice, we generally replace m_{ij} with a lumped, diagonal mass matrix so that Eq. (3) becomes

$$m_i \mathbf{v}_i = \sum_p m_p \mathbf{v}_p N_i(\mathbf{x}_p) \quad (6)$$

where lumped mass is

$$m_i = \sum_p m_p N_i(\mathbf{x}_p) \quad (7)$$

After the information is mapped from material particles to mesh nodes, the discrete formulation of Eq. (2) on the mesh nodes can be obtained, as described below.

The weak form of Eq. (2) can be found, based on the standard procedure used in the finite element method,

$$\int_{\Omega} \rho \delta \mathbf{v} \cdot d\mathbf{v} / dt d\Omega + \int_{\Omega} \delta(\mathbf{v} \nabla) \cdot \boldsymbol{\sigma} d\Omega - \int_{\Gamma_t} \delta \mathbf{v} \cdot \mathbf{t} d\Gamma - \int_{\Omega} \rho \delta \mathbf{v} \cdot \mathbf{b} d\Omega = 0. \quad (8)$$

where Ω is the domain to be solved, Γ_t is the traction boundary, $\boldsymbol{\sigma}$ is the stress tensor, \mathbf{t} is the external force vector and \mathbf{b} is the body force vector.

Since the continuum bodies is described with the use of a finite set of material particles, the mass density can be written as,

$$\rho(\mathbf{x}) = \sum_{p=1}^{N_p} m_p \delta(\mathbf{x} - \mathbf{x}_p) \quad (9)$$

where δ is the Dirac delta function with dimension of the inverse of volume. The substitution of Eq. (9) into Eq. (??) converts the integral to the sums of quantities evaluated at the material particles, namely,

$$m_i \frac{d\mathbf{v}_i}{dt} = (\mathbf{f}_i)^{\text{int}} + (\mathbf{f}_i)^{\text{ext}} \quad (10)$$

where m_i is the lumped mass, $(\mathbf{f}_i)^{\text{int}}$ and $(\mathbf{f}_i)^{\text{ext}}$ are the external force vector and internal force vector which read separately

$$(\mathbf{f}_i)^{\text{int}} = - \sum_p^{N_p} m_p \sigma \cdot (\nabla N_i) / \rho_p, \quad (11)$$

$$(\mathbf{f}_i)^{\text{ext}} = \sum_{p=1}^{N_p} N_i \mathbf{b}_p + \mathbf{f}_i^c \quad (12)$$

where the vector \mathbf{f}_i^c is the contact force which is the external nodal force not including the body force and is illustrated in the following section.

An explicit time integrator is used to solve Eq. (10) for the nodal accelerations, with the time step satisfying the stability condition. The critical time step is the ratio of the smallest cell size to the wave speed. After the equations of motion are solved on the cell nodes, the new nodal values of acceleration are used to update the velocity of the material particles. The strain increment for each material particle is determined with the use of gradient of the nodal basis function evaluated at the material particle position. The corresponding stress increment can be found from the constitutive model. The internal state variables can also be completely updated. The computational mesh may be discarded, and a new mesh is defined, if desired for the next time step. As a result, an effective computational mesh could be chosen for convenience.

III. THE CONTACT ALGORITHM

The MPM with a natural no-slip contact algorithm is based on a common background mesh. As a result, it is impossible to separate the contacting bodies. Bardenhagen et al.[13, 14] have proposed a contact algorithm in which the contact between bodies is handled when the velocity field of an individual particle differs from the single, center-of-mass velocity field in the cell containing contacting particles. Their contact algorithm was incorporated into the MPM to simulate the interactions in granular materials based on the velocity field.

In this section, we will improve the multi-mesh contact algorithm which recovers more faithfully the opposite acting forces between contacting bodies. In MPM, several bodies may be mapped on to the same nodes of the background mesh, so it is necessary to define a multi-value of velocity and mass on every node. In practice, it is impossible that the number of values defined at one node is as many as the number of bodies, otherwise the memory of computer will be too much wasted if there are thousands of bodies to be simulated. In this paper we

define four values on every node. That is to say, there are at most four bodies mapped on to the same nodes, although there can be thousands of bodies in the whole domain. In that case, each node has a mesh mass m_i^g and momentum \mathbf{P}_i^g associated with it, where g ranges from one to four and the mesh velocity \mathbf{v}_i^g can be obtained from the mesh momentum and the mass,

$$\mathbf{v}_i^g = \mathbf{P}_i^g / m_i^g \quad (13)$$

Note that if the mesh mass m_i^g is close to zero, the obtained mesh velocity maybe singular which will cause error during the calculations. In this paper, to avoid the singularity, the shape function is altered, if ξ , η or ζ is small than -0.99 or larger than 0.99 that means the material point is too close to the node, ξ , η or ζ is adjusted to -0.99 or 0.99 . Since the shape functions have compact support, only those nodes in the vicinity of the bodies will have a meaningful velocity and the body velocity at other nodes will be zero.

Obviously, if the momenta of two bodies are projected on to the same node, the contact may occur and the contact between bodies r and s is directed by comparing the fields \mathbf{v}_i^r and \mathbf{v}_i^s which are determined by using mass weighting given in Eq. (13),

$$(\mathbf{v}_i^r - \mathbf{v}_i^s) \cdot \mathbf{n}_i^{rs} > 0, \quad (14)$$

where \mathbf{n}_i^{rs} is the unit outward normal at node i along the boundary. Multiply Eq. (14) with $m_i^r m_i^s$, it can be written as,

$$(m_i^s \mathbf{P}_i^r - m_i^r \mathbf{P}_i^s) \cdot \mathbf{n}_i^{rs} > 0 \quad (15)$$

If Eq. (14) is satisfied, the velocities of body r and body s are adjusted to new values $\bar{\mathbf{v}}_i^r$ and $\bar{\mathbf{v}}_i^s$ so that

$$\bar{\mathbf{v}}_i^r \cdot \mathbf{n}_i^{rs} = \bar{\mathbf{v}}_i^s \cdot \mathbf{n}_i^{rs} \quad (16)$$

holds. That is, the normal components of velocity of body r and body s are set to be equal. Eq. (16) can also be written as

$$m_i^s \bar{\mathbf{P}}_i^r \cdot \mathbf{n}_i^{rs} = m_i^r \bar{\mathbf{P}}_i^s \cdot \mathbf{n}_i^{rs}. \quad (17)$$

As a reasonable contact algorithm, the momentum is required to be unaltered, i.e.,

$$(\mathbf{P}_i^r + \mathbf{P}_i^s) \cdot \mathbf{n}_i^{rs} = (\bar{\mathbf{P}}_i^r + \bar{\mathbf{P}}_i^s) \cdot \mathbf{n}_i^{rs} \quad (18)$$

From Eqs. (17) and (18) the updated mesh momenta are obtained,

$$\bar{\mathbf{P}}_i^r = \mathbf{P}_i^r - (m_i^s \mathbf{P}_i^r - m_i^r \mathbf{P}_i^s) \cdot \mathbf{n}_i^{rs} \mathbf{n}_i^{rs} / (m_i^r + m_i^s), \quad (19)$$

$$\bar{\mathbf{P}}_i^s = \mathbf{P}_i^s + (m_i^s \mathbf{P}_i^r - m_i^r \mathbf{P}_i^s) \cdot \mathbf{n}_i^{rs} \mathbf{n}_i^{rs} / (m_i^r + m_i^s). \quad (20)$$

So the updated mesh velocities are:

$$\bar{\mathbf{v}}_i^r = \mathbf{v}_i^r - m_i^s (\mathbf{v}_i^r - \mathbf{v}_i^s) \cdot \mathbf{n}_i^{rs} \mathbf{n}_i^{rs} / (m_i^r + m_i^s), \quad (21)$$

$$\bar{\mathbf{v}}_i^s = \mathbf{v}_i^s + m_i^r (\mathbf{v}_i^r - \mathbf{v}_i^s) \cdot \mathbf{n}_i^{rs} \mathbf{n}_i^{rs} / (m_i^r + m_i^s). \quad (22)$$

Especially, if body s is a rigid wall, we set the value of m_i^s much larger than that of m_i^r . Thus Eq. (21) and Eq. (22) can be reduced to:

$$\bar{\mathbf{v}}_i^r = \mathbf{v}_i^r - (\mathbf{v}_i^r - \mathbf{v}_i^s) \cdot \mathbf{n}_i^{rs}, \quad (23)$$

$$\bar{\mathbf{v}}_i^s = \mathbf{v}_i^s, \quad (24)$$

Obviously, the velocity of rigid body s is not altered during the contact.

The equations (21) and (22) determining the velocities are identical to that by Bardenhagen[13] and in practice they are same, but the calculation of the normal and tangential contact forces makes the difference which will be described as following are different.

Once bodies r and s contact, they move together along the normal until they separate when the contact condition expressed in Eq. (15) is not satisfied. So the acceleration along the normal of body r is equal to that of s during the course of the contact. That is

$$\mathbf{a}_i^r \cdot \mathbf{n}_i^{rs} = \mathbf{a}_i^s \cdot \mathbf{n}_i^{rs} \quad (25)$$

where \mathbf{a}_i^r and \mathbf{a}_i^s are the accelerations of bodies r and s at node i , respectively. They can be obtained from the Newtonian second law,

$$m_i^r(\mathbf{a}_i^r \cdot \mathbf{n}_i^{rs}) = \mathbf{f}_i^{r,int} \cdot \mathbf{n}_i^{rs} - f_i^{nor} \quad (26)$$

$$m_i^s(\mathbf{a}_i^s \cdot \mathbf{n}_i^{rs}) = \mathbf{f}_i^{s,int} \cdot \mathbf{n}_i^{rs} + f_i^{nor} \quad (27)$$

where f_i^{nor} is the normal contact force between body r and body s at node i , which can be obtained from Eq. (25)–(27),

$$f_i^{nor} = (m_i^s \mathbf{f}_i^{r,int} - m_i^r \mathbf{f}_i^{s,int}) \cdot \mathbf{n}_i^{rs} / (m_i^r + m_i^s) \quad (28)$$

Note that the normal contact force must be nonnegative. So once f_i^{nor} is negative, it is set to be zero. That is

$$f_i^{nor} = \begin{cases} \Psi / (m_i^r + m_i^s), & \Psi \geq 0 \\ 0, & \Psi < 0 \end{cases} \quad (29)$$

where $\Psi = (m_i^s \mathbf{f}_i^{r,int} - m_i^r \mathbf{f}_i^{s,int}) \cdot \mathbf{n}_i^{rs}$. For the cases f_i^{nor} in Eq. (28) is positive, the contacting bodies at time t may still contact in the next time step although the criterion of contact in Eq.(15) is not satisfied, so the contact condition should be applied in the next time step.

The contact force in the Bardenhagen's contact algorithm is calculated as

$$f_i^{r,nor} = m_i^r [(\tilde{\mathbf{v}}_i - \mathbf{v}_i^r) \cdot \mathbf{n}_i^{rs}] / \Delta t \quad (30)$$

where $\tilde{\mathbf{v}}_i$ is the center-of-mass velocity at node i . Actually, the normal contact force may still be very large even if the normal velocities of different bodies at contact nodes are same during the course of contacting. The normal contact force calculated by (30) is not physical and may cause numerical energy dissipation which will be shown in the next section.

When without friction, the contact algorithm has been finished up to now. In the case with friction, the frictional slip is accomplished by adjusting the tangential component. To

apply Coulomb friction, we first calculate the force necessary to cause the bodies to stick together completely. Again, the comparison of the mesh velocity of body r to that of body s provides exactly the correct constraint for no-slip contact if body r and body s contact, the relative tangential velocity is

$$(\mathbf{v}_i^r - \mathbf{v}_i^s) \cdot \mathbf{s}_i^r \quad (31)$$

where \mathbf{s}_i^r is the unit tangential at node i along the boundary,

$$\mathbf{s}_i^r = ((\mathbf{v}_i^r - \mathbf{v}_i^s) - (\mathbf{v}_i^r - \mathbf{v}_i^s) \cdot \mathbf{n}_i^{rs} \mathbf{n}_i^{rs}) / |((\mathbf{v}_i^r - \mathbf{v}_i^s) - (\mathbf{v}_i^r - \mathbf{v}_i^s) \cdot \mathbf{n}_i^{rs} \mathbf{n}_i^{rs})| \quad (32)$$

To get an appropriate frictional force allowing slip, we start from the non-slip condition. The tangential velocities of body r and body s must be set to be equal after one time step Δt . Suppose the tangential contact force is f_i^{tang} . It should satisfy

$$(\mathbf{P}_i^r \cdot \mathbf{s}_i^r + (\mathbf{f}_i^{r,\text{int}} \cdot \mathbf{s}_i^r - f_i^{\text{tang}}) \Delta t) / m_i^r = (\mathbf{P}_i^s \cdot \mathbf{s}_i^r + (\mathbf{f}_i^{s,\text{int}} \cdot \mathbf{s}_i^r + f_i^{\text{tang}}) \Delta t) / m_i^s. \quad (33)$$

Then the needed constraining tangential force f_i^{tang} is

$$f_i^{\text{tang}} = ((m_i^s \mathbf{P}_i^r - m_i^r \mathbf{P}_i^s) + (m_i^s \mathbf{f}_i^{r,\text{int}} - m_i^r \mathbf{f}_i^{s,\text{int}}) \Delta t) \cdot \mathbf{s}_i^r / ((m_i^r + m_i^s) \Delta t) \quad (34)$$

The expected frictional force should equal to f_i^{tang} if the latter is small, and be proportional to the magnitude of the normal force and independent of the contact area if f_i^{tang} exceed a specified value. That is to say, the frictional force just balances the tangential force to prevent relative tangential motion when the latter is small. When the latter is large, we limit the frictional force to have a magnitude less than it to allow tangential slip between the contacting bodies. The direction of the frictional force is chosen as in (32) to oppose the relative motion. Putting these requirements together yields,

$$f_i^{\text{fric}} = \min(\mu f_i^{\text{nor}}, f_i^{\text{tang}}). \quad (35)$$

where μ is the coefficient of friction. To complete the formulation of the contact algorithm, a value \mathbf{n}_i^{rs} of the normal at node i of the computational mesh for the contacting bodies r and s is still needed. As an approximation, the following algorithm is presented to determine the normal value,

1. If bodies r and s contact at node i , initialize vectors \mathbf{V}_r and \mathbf{V}_s as zero.
2. Search within the eight cells(for three-dimensional cases) around the node. If cell j possesses particles belonging to body r (or s), calculate the difference of coordinates between the node i and the center of cell j , $\mathbf{x}_i - \mathbf{x}_c^j$, then add the difference to vector \mathbf{V}_r (or \mathbf{V}_s).
3. Calculate the difference between the vectors \mathbf{V}_r and \mathbf{V}_s , then set the difference as the value of \mathbf{n}_i^{rs} . Finally, unitize \mathbf{n}_i^{rs} .

Finally, we summarize the material point method with the new multi-mesh contact algorithm presented in this paper as follows:

1. Get the particle mass m_r , position \mathbf{x}_r , velocity \mathbf{v}_r , density ρ_r , and stress σ ; form the lumped mass matrix(Eq. (7)) and nodal momentum(Eq. (6)).
2. Loop over the mesh nodes, if two bodies contact at node i , adjust the nodal momenta of the contacting bodies(Eq. (19), Eq. (20)).
3. Calculate the rate of the deformation gradient for each particle, compute the increment of strain using an appropriate strain measure and solve constitutive equations to update the stress, σ_p .
4. Form the internal force (Eq. (11)). Calculate the contact force between bodies and form the external force(Eq. (12))
5. Solve the momentum equations for the nodal accelerations and get the velocity in a Lagrangian frame:

$$m_i[\mathbf{v}_i|_{t+\Delta t} - \mathbf{v}_i|_t] = \Delta t[(\mathbf{f}_i)^{\text{int}} + (\mathbf{f}_i)^{\text{ext}}] \quad (36)$$

6. Update the solution at the material point by mapping the nodal values using the element shape functions. Positions and velocities are updated according to

$$\mathbf{x}_p|_{t+\Delta t} = \mathbf{x}_p|_t + \Delta t \sum_i \mathbf{v}_i|_{t+\Delta t} N_i(\mathbf{x}_p) \quad (37)$$

and

$$\mathbf{v}_p|_{t+\Delta t} = \mathbf{v}_p|_t + \sum_i [\mathbf{v}_i|_{t+\Delta t} - \mathbf{v}_i|_t] N_i(\mathbf{x}_p) \quad (38)$$

7. Define a new finite element mesh if necessary, and return to step 1 to begin a new time step.

IV. NUMERICAL SIMULATION

Numerical simulations presented in this section are carried out in three dimension. The first set of simulation involves a cylinder rolling on an inclined rigid plane and is meant as simple illustration and validation of the friction algorithms presented by Bardenhagen et al. and by us. The second set involves the collision of two elastic spheres and is to examine the efficiency of the multi-mesh contact algorithm proposed in this paper. The third set involves a copper Taylor bar impacting to a rigid wall. The last example is to simulate the process of the collision between four identical spheres. The last two examples examine the conservation of energy during the collision is checked.

A. Rolling simulation

Fig 1 shows the plane geometry for a computation with a cylinder on an inclined plane. In this example, the plane inclined at an angel θ with respect to the horizontal line, while the gravity \mathbf{g} is vertically downward.

FIG. 1: Geometry for simulations of a cylinder on an inclined plane

A rigid cylinder on an inclined surface will roll, or slip depending on the angle of inclination and friction coefficient. Specifically, if $\tan \theta > 3\mu$, the cylinder will roll and slip; Otherwise the cylinder will roll without slipping, where μ is the coefficient of friction. For an initially stationary, rigid cylinder, the x -component and the center-of-mass position as a function of time, $x_{\text{cm}}(t)$, is given by

$$x_{\text{cm}}(t) = \begin{cases} x_0 + \frac{1}{2}|\mathbf{g}|t^2(\sin \theta - \mu \cos \theta), & \tan \theta > 3\mu \quad (\text{slip}), \\ x_0 + \frac{1}{3}|\mathbf{g}|t^2 \sin \theta, & \tan \theta \leq 3\mu \quad (\text{stick}), \end{cases} \quad (39)$$

In Eq. (39), x_0 is the x -component of the initial center-of-mass position, and $|\mathbf{g}|$ is the magnitude of the gravitational acceleration.

Simulation is performed with a cylinder that has the radius $R = 40\text{mm}$, thickness $t = 20\text{mm}$, and gravitational acceleration with magnitude 10m/s^2 . The computational domain is cubic with side length length 700mm, 150mm and 40mm, respectively. The cell size is 10mm so there are only eight and two computational elements across the diameter and the thickness of the cylinder, respectively. The simulation involves a elastic, deformable cylinder with elastic modulus 1.24MPa, Poisson ratio 0.35 and density $8.0 \times 10^{-3}\text{g/mm}^3$. The inclined plane is discretized as a rigid body with 70, 15 and 4 material points, respectively, and there is only one material point in one cell.

Fig. 2 shows the center-of-mass position of the cylinder as a function of time for three values of angel of inclination, $\theta = \pi/12$, $\theta = \pi/6$ and $\theta = \pi/4$, respectively, and the coefficient of friction fixed at $\mu = 0.5$. The symbols represent simulation results, and lines represent analytical ones. Fig. 2(a) shows the results of our contact algorithm while Fig. 2(b) shows those of contact algorithm by Bardenhagen. For cases with large inclination angle the results of both contact algorithms agree well with analytical solutions. But when the inclination angle is small, results of our contact algorithm are much better.

In the next test, the value of angle of inclination is fixed at $\theta = \pi/6$ and the coefficient of friction is varied, $\mu = 0.1$ and $\mu = 0.5$. Fig. 3 shows the center-of-mass position of the cylinder as a function of time for each simulation and the corresponding exact solution for a rigid cylinder. The computed results for the deformable cylinders agree well with the analytical solutions, and as before, the computed curves obtained with our contact algorithm are much more closer to the analytical curves than those by Bardenhagen's algorithm.

Fig. 4 shows simulation results for different mesh sizes. In this test, the angle of inclination is fixed at $\theta = \pi/6$ and the coefficient of friction is fixed at $\mu = 0.5$. The side length of the cubic computational elements is varied, 40mm, 20mm and 10mm, respectively. Fig. 4(a) shows the results of our contact algorithm while Fig. 4(b) shows those of Bardenhagen's. It is clear that the simulation results converge to the analytical ones with the decrease of the mesh size. The agreement between results by our contact algorithm agree better with analytical ones than those by Bardenhagen's scheme in the later time.

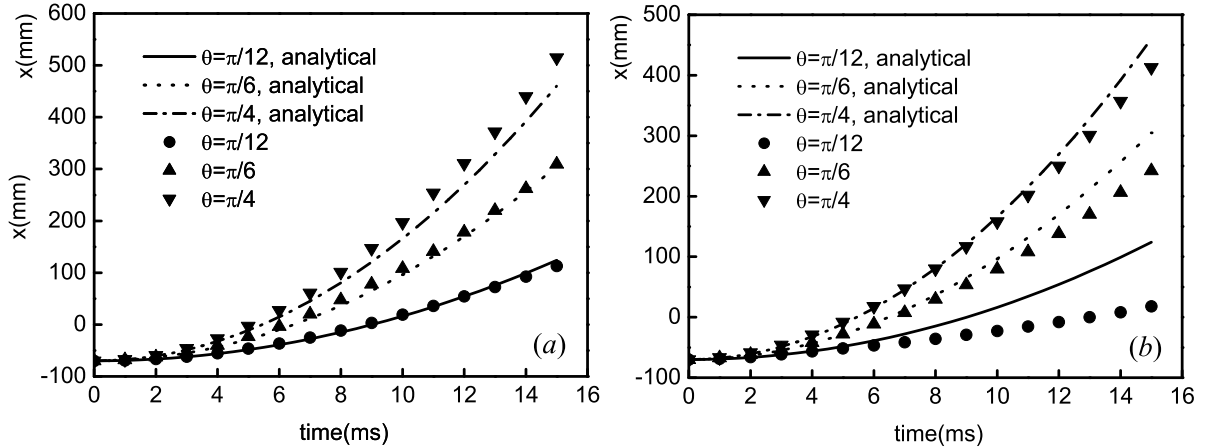


FIG. 2: Center-of-mass position for deformable cylinder vs time. The coefficient of friction, $\mu = 0.5$, the angles of inclination, $\theta = \pi/12, \pi/6$ and $\pi/4$, respectively. The symbols represent simulation results while lines represent analytical ones. (a) our contact algorithm, (b) contact algorithm by Bardenhagen.

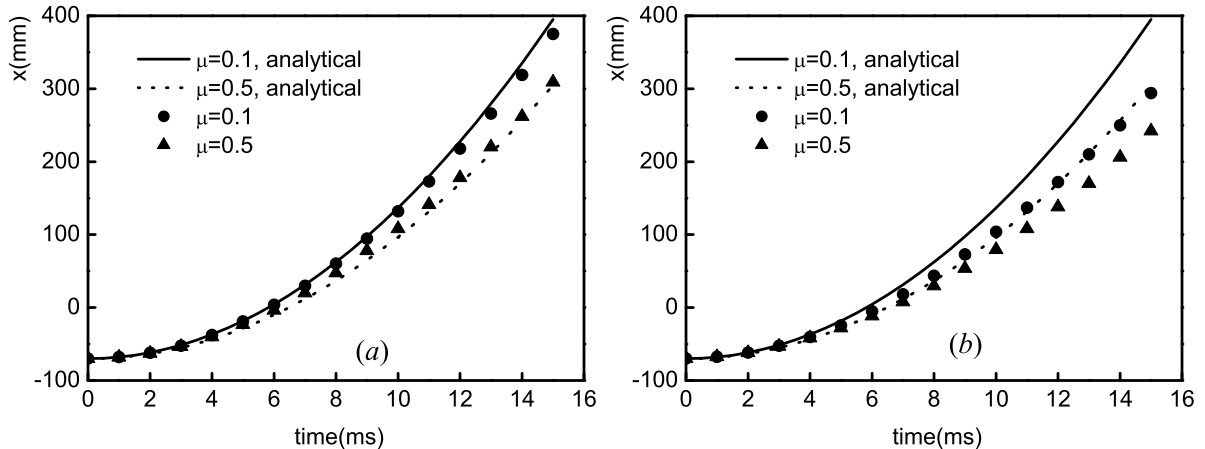


FIG. 3: Center-of-mass position for deformable cylinder as a function of time. The angle of inclination, $\theta = \pi/6$, and coefficient of friction, $\mu = 0.1, 0.5$, respectively. The symbols represent simulation results while lines represent analytical ones. (a) our contact algorithm, (b) algorithm by Bardenhagen.

B. Impact of elastic spheres

In this section, the impact of two elastic spheres is simulated to test the conservation of the energy during the impact with the contact algorithm. The variables are all dimensionless in this example. The spheres start from the left side and the center of the computational

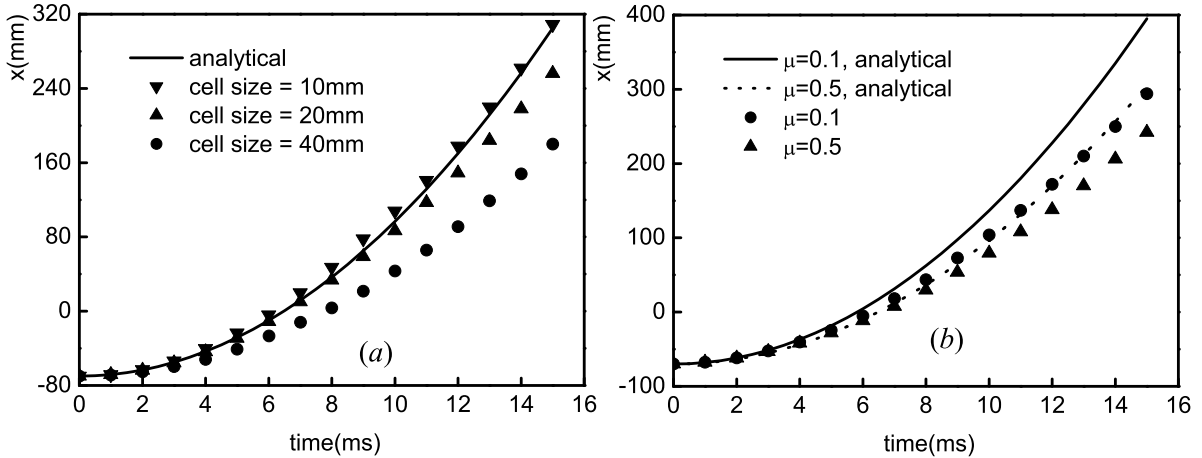


FIG. 4: Center-of-mass position for deformable cylinder as a function of time. In the simulation angle of inclination is $\theta = \pi/6$, coefficient of friction is $\mu = 0.5$ and side lengths of cells are 40mm, 20mm and 10mm, respectively. (a) our algorithm, (b) algorithm by Bardenhagen.

FIG. 5: Snap-shots of impact of two elastic spheres obtained by our contact algorithm. From up to down, the corresponding times are 0ms, 37.8ms and 75.0ms, respectively.

domain with initial velocities $(0.1, 0, 0)$ and $(0, 0, 0)$, respectively. The computational domain is a cube whose sides along the x , y and z direction are 40, 20 and 20, respectively, and cubic meshes are used with side length $\Delta x = \Delta y = \Delta z = 0.5$. Eight material points are used per element. The spheres have a radius of 4, Young's modulus of 1000, a Poisson's ratio of 0.3 and a density of 1.0. The distance between the center of first sphere and that of the second sphere is 14. The simulation is run up to a final time $t = 80$.

The results from our contact algorithm are shown in Fig.5. As a comparison, the results from the contact algorithm by Bardenhagen are shown in Fig.6. In order to show the moving of spheres clearly, only the central layer of the 3D configuration is shown. The nonlinear constitution for large-deformation is used. In these figures, (a) show the two spheres at time $t = 0.0$ when they just begin to travel through the grid, (b) show the impact of spheres at time $t = 37.8$ and (c) show the spheres at time $t = 75.0$. From Fig.5 (c) we find two spheres separate, and the left one is almost immobile and the right one moves with nearly the same kinetic energy as the initial kinetic energy of left one. But in Fig.6 (c) the two spheres move forward together, which is unphysical.

Fig.7 shows the kinetic, potential and total energies as a function of time in which (a) shows the results of our contact algorithm while (b) shows those of Bardenhagen's. From Fig. 7(a)

FIG. 6: Snap-shots of impact of two elastic spheres obtained by Bardenhagen's contact algorithm. From up to down, the corresponding times are 0ms, 37.8ms and 75.0ms, respectively.

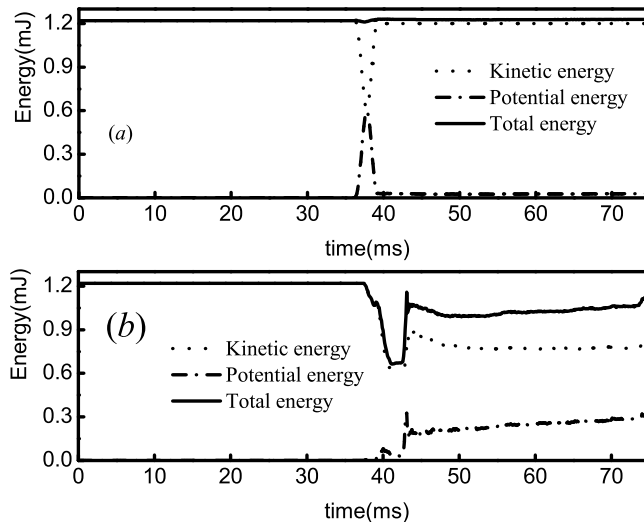


FIG. 7: Energy evolution of elastic cylinder impact. The results with the contact algorithms presented in this paper and by Bardenhagen are shown in (a) and (b), respectively.

we find the kinetic energy decreases during the impact and recovers after the spheres separate. The potential energy (broken line) begin to accumulate upon impact of spheres, reaches its maximum value at the point with maximum deformation during impact, then decreases to a small mount associated with the free vibration of the spheres after separation. The total energy(solid line) is approximately constant. In Fig. 7(b), the kinetic energy decreases during the impact but doesn't recover to the original one; the potential energy begin to increase when the contact begins, then reaches its a maximum value, and does not decrease. Total energy shown in Fig. 7(b) is not constant, which shows a strong numerical dissipation during the course of impact.

C. Impact of a Taylor Bar

The classical Taylor bar problem is considered. This is a commonly simulated problem and is often used as a benchmark for transient dynamics computer codes. A copper bar of radius $R = 3.8\text{mm}$ and length $L_0 = 25.4\text{mm}$ impacts on a rigid, frictionless wall with an initial longitudinal velocity of 190m/s . The material is modeled as elastoplastic with Young's modulus $E = 117\text{GPa}$, Poisson $\nu = 0.35$, the yield stress is $\sigma_y = 0.157\text{MPa}$ and linear hardening is assumed with $H = 0.425\text{MPa}$. The material has a density of $\rho_0 = 8.93\text{g/cm}^3$. In order to compare the computed results to those of experiments, we use the following estimation of error given by G. R. Johnson[19]:

$$\bar{\Delta} = \frac{1}{3} \left(\frac{|\Delta L|}{L} + \frac{|\Delta D|}{D} + \frac{|\Delta W|}{W} \right) \quad (40)$$

FIG. 8: The sketch figure of the impact of a Taylor bar

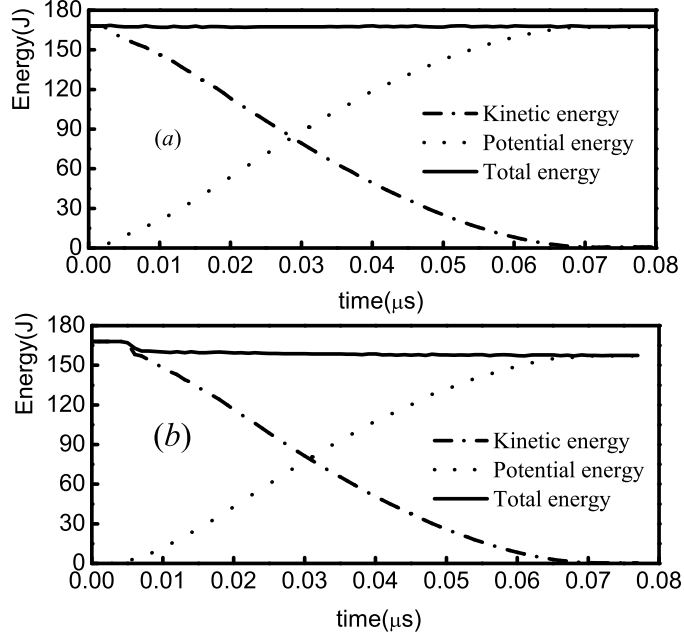


FIG. 9: Energy evolution during impact of Taylor bar

where L and D are the length and diameter of the bottom after the impact, respectively, as shown in Fig. 8. W is the diameters of the layer which is $0.2L_0$ to the bottom.

The bar moves within the cubic domain $[-10.4, 10, 4] \times [-10.4, 10, 4] \times [-2, 36]$, meshed by $30 \times 30 \times 50$ elements. For the initial construction of the bar, there are 8 material points in every cell, and for the rigid wall there is only one material point. The unit of coordinate is millimeter. The terminal time is $80\mu s$. Fig. 9 shows the kinetic, potential and total energy as a function of time, where the contact algorithm presented by us (Fig. 9(a)) and by Badenhagen (Fig. 9(b)) are used. In Fig. 9(a), the kinetic energy decreases during the impact and is totally converted to potential energy at the end. The total energy is constant during the whole time. In Fig. 9(b), the energy is dissipated during the impact.

Table I shows the comparison between the computed results and experimental ones, where MPM1 is MPM with our contact algorithm and MPM2 is MPM with contact algorithm presented by Bardenhagen. The results by MPM1 agree better with experimental ones.

Fig. 10 shows the final particle configuration, colored by contour values of equivalent plastic strain obtained with MPM1. Fig. 10(a) shows three-dimensional view while Fig. 10(b) shows the center layer of Fig. 10(a) vertically to the rigid wall.

FIG. 10: The final particle configuration of the Taylor bar

TABLE I: The comparison between the computed results and experimental ones

	L(mm)	D(mm)	W(mm)	$\bar{\Delta}$
Experiment	16.2	13.5	10.1	-
MPM1	16.15	13.21	9.63	0.071
MPM2	16.25	11.96	9.42	0.184

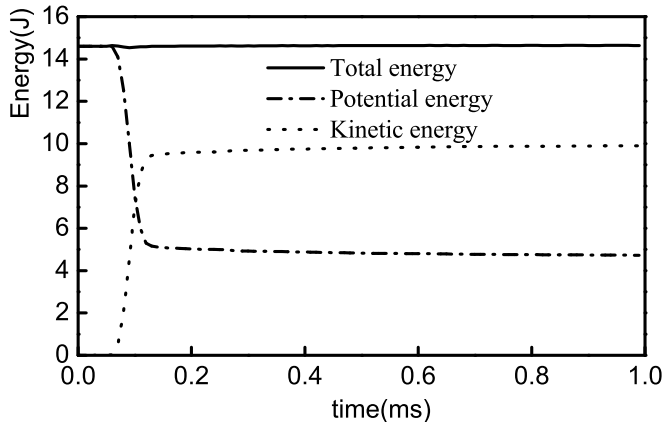


FIG. 11: Energy evolution during impact of four copper spheres.

D. Impact of plastic spheres

The last example simulates the impact of four identical copper spheres with the contact algorithm presented in this paper. The material parameters of spheres are the same as those of last example. The radius of the spheres is 10mm. Initially, one of the spheres locates at $(0.0, 0.0, 25.0)$ and travels with a velocity -100m/s parallel to the z axis; The other three spheres locate at $(10, -5.7735, 0.0)$, $(0.0, 11.547, 0.0)$ and $(-10.0, -5.7735, 0.0)$ are at rest. The unit of coordinate is millimeter.

The spheres moves within the cubic domain $[-50, 50] \times [-50, 50] \times [-50, 50]$, meshed by $50 \times 50 \times 50$ elements. Fig. 11 shows the kinetic, potential and total energy as a function of time. The kinetic energy decreases during the impact and part of the kinetic energy is converted to potential energy during the impact. The total energy is a constant during the whole time.

Fig.12(a)–(c) show the particle configurations of different time, colored by contour value of equivalent plastic strain. From blue to red the plastic strain increases and correspondingly the possible temperature increment becomes larger. Fig. 12(a) shows the initial particle configuration at $t = 0\mu\text{s}$. Fig. 12(b) shows the particle configuration at $t = 80\mu\text{s}$ when the

FIG. 12: Snapshots of impact of four copper spheres. From black to white the plastic strain increases and correspondingly the possible temperature increment becomes larger. (a) $t = 0\mu s$; (b) $t = 80\mu s$; and (c) $t = 1ms$

upper sphere just impact to the lower three ones. Fig. 12(c) show the particle configuration at $t = 1ms$ when they separate.

V. CONCLUSION

A new multi-mesh contact algorithm for three-dimensional material point method is presented. The contact algorithm faithfully recovers the opposite acting forces between colliding bodies. Collision procedures between regular bodies and/or rigid bodies can be treated within the same framework. A multi-value of momentum and mass is defined on every node to describe the contact/sliding/separation procedure. Both normal and tangential velocities of each particle at the contact surface are calculated in respective individual mesh. A Coulomb friction is applied to describe the sliding or slipping between the contacting bodies. The efficiency of the contact algorithm is linearly related to the number of the contacting bodies because the overlapped nodes are labeled by sweeping the material particles of all bodies when the nodal momentum and mass are formed in every time step.

Numerical simulation shows that our contact algorithm possesses high accuracy and low numerical energy dissipation, which is very important for solving collision problems.

Acknowledgments

We warmly thank G. Bardenhagen, Haifeng Liu, Song Jiang, Xingping Liu, Xijun Yu, Zhijun Shen, Yangjun Ying, Guoxi Ni, and Yun Xu for helpful discussions.

-
- [1] J. U. Brackbill, H. M. Ruppel, *J. Comput. Phys.* **65**(1986)314.
 - [2] J. U. Brackbill, D. B. Kothe, H. M. Ruppel, *Comput. Phys. Comm.* **48**(1988)25.
 - [3] D. Sulsky, Z. Chen, H. L. Schreyer, *comput Methods Appl. Mech. Engrg.* **118**(1994)179.
 - [4] Z. Chen, W. Hu. L. Shen, X. Xin, R. Brannon, *Engineering Fracture Mechanics.* **69**(2002)1873.
 - [5] Z. Chen, R. Feng. X. Xin and L. Shen, *Int. J. Numer. Meth. Engrg.* **56**(2003)1979.
 - [6] D. Sulsky, J. U. Brackbill, H. L. Schreyer, *Comput. Phys. Comm.* **87**(1995)236.
 - [7] Z. Wiechowski, *Comput Methods Appl. Mech. Engrg.* **193**(2004)4417.
 - [8] C. J. Coetzee, P. A. Vermeer and A. H. Basson, *Int. J. Numer. Anal. Meth. Geomech.* **29**(2005)879.
 - [9] X. Zhang, K. Y. Sze, S. Ma, *Int. J. Numer. Meth. Engrg.* **66**(2006)689.

- [10] Allen R. York II, Deborah Sulsky and Howard L. Schreyer, *Int. J. Numer. Meth. Engrg.* **44**(1999)1429.
- [11] Honglai Tan, John A. Nairn, *Comput. Methods Appl. Mech. Engrg.* **191**(2002)2095.
- [12] Joris J. C. Remmers, René, Alan Needleman, VIII International Conference on Computational Plasticity, Barcelona, 2005.
- [13] S. G. Bardenhagen, J. U. Brackbill, D. Sulsky, *Comput Methods Appl. Mech. Engrg.* **187**(2000)529.
- [14] S. G. Bardenhagen, J. E. Guilkey and K. M. Roessig and J. U. Brackbill and W. M. Witzel and J. C. Foster. *Comput Methods Appl. Mech. Engrg.* **Vol 2, n4**(2001)529.
- [15] S. J. Cummins and J. U. Brackbill, *J. Comput. Phys.* **180**(2002)506.
- [16] S. G. Bardenhagen and J. U. Brackbill, *Journal of Applied Physics.* **83**(1998)5732.
- [17] S. G. Bardenhagen and J. U. Brackbill, *Physical Review E.* **62**(2000)3882.
- [18] W. Hu, Z. Chen, *Computers and structures* **81**(2003)1991.
- [19] G. R. Johnson, T. J. Holmquist, *J. Appl. Phys.* **64**(1988)3901.

This figure "Fig1.jpg" is available in "jpg" format from:

<http://arxiv.org/ps/0708.3532v1>

This figure "Fig5.jpg" is available in "jpg" format from:

<http://arxiv.org/ps/0708.3532v1>

This figure "Fig6.jpg" is available in "jpg" format from:

<http://arxiv.org/ps/0708.3532v1>

This figure "Fig10.jpg" is available in "jpg" format from:

<http://arxiv.org/ps/0708.3532v1>

This figure "Fig12.jpg" is available in "jpg" format from:

<http://arxiv.org/ps/0708.3532v1>